Low-temperature carburizing improves hydrogen embrittlement resistance of cold worked 304 austenitic stainless steel

Citation for the original published paper (version of record):
Qin, X., Nyborg, L., Liu, H. et al (2025). Low-temperature carburizing improves hydrogen embrittlement resistance of cold worked 304
austenitic stainless steel. Journal of Materials Research and Technology, 36: 8816-8825.
http://dx.doi.org/10.1016/j.jmrt.2025.05.125

Journal of Materials Research and Technology 36 (2025) 8816–8825

Contents lists available at ScienceDirect

Journal of Materials Research and Technology

journal homepage: www.elsevier.com/locate/jmrt

Low-temperature carburizing improves hydrogen embrittlement resistance of cold worked 304 austenitic stainless steel

Xiao Qin [a,b], Lars Nyborg [a], Huiqun Liu [b], Alexandra Bauer [c], Yu Cao [a,*]

[a] Department of Industrial and Materials Science, Chalmers University of Technology, Gothenburg, 41296, Sweden
[b] School of Materials Science and Engineering, Central South University, Changsha, 410083, PR China
[c] Bodycote Specialist Technologies GmbH, 86899, Landsberg, Germany

ARTICLE INFO

Keywords:
Low-temperature carburizing
Austenitic stainless steel
Hydrogen embrittlement
Expanded austenite

ABSTRACT

Cold deformation-induced martensitic transformation in 304 austenitic stainless steel (ASS) increases its susceptibility to hydrogen embrittlement (HE). In this study, low-temperature carburizing (LTC) was performed on cold worked 304 ASS. Its effect on the mechanical properties and HE was investigated by electrochemical cathodic hydrogen charging and slow strain rate tensile test. Microstructure, fractography, and hydrogen uptake were analyzed to examine the hydrogen-induced failure. It has been found that LTC introduced the expanded austenite on the steel surface, which increased strength and surface hardness but reduced the elongation. LTC increased the initial strain hardening rate and suppressed strain-induced martensitic transformation, showing higher strain rate sensitivity. Hydrogen uptake caused loss of ductility and formation of a quasi-cleavage layer with some cracks on the surface of the steel. The HE resistance was significantly improved by LTC treatment. Cold-worked 304 showed a higher HE index due to the martensitic transformation and a higher hydrogen concentration. The remarkably reduced susceptibility to HE by LTC treatment was attributed to the carbon stabilized austenite and consequently inhibited martensite transformation, as well as compressive stress in the expanded austenite. These factors reduce hydrogen diffusion and hydrogen uptake.

1. Introduction

Austenitic stainless steels (ASS) are the preferred structural materials of choice for hydrogen storage and transport [1] due to their low hydrogen diffusion coefficient [2,3] and excellent resistance to hydrogen embrittlement (HE) [4,5]. Austenite-stabilizing elements (such as nickel) are costly in ASS. This makes metastable AISI 304 with low Ni content attractive for hydrogen applications from an economic point of view. However, the low yield strength of 304 ASS requires work hardening to improve its mechanical properties [6–8]. The phase transformation from γ-austenite to α'-martensite in a metastable ASS due to plastic deformation can greatly increase its susceptibility to HE [9–11]. Premature fracture of metallic materials caused by HE is an unexpected catastrophic failure.

Reducing hydrogen diffusion or introducing hydrogen traps [12–17] are two potentially effective strategies to improve HE resistance. Some efforts have been made. Kim et al. [14] found that increasing nitrogen content in Fe–15Cr–15Mn–4Ni-0.3Si alloy could reduce hydrogen diffusion and consequently decrease susceptibility to HE in ASS. It has been reported that HE resistance of 304 ASS can be improved by refined grain size by heat treatment [15], and tailored deformation structure by controlling the rolling temperature [16]. The former, i.e., refined grain size, alleviated strain localization, which might otherwise act as a high-velocity channel for hydrogen diffusion to initiate a crack. The latter, tailored deformation structure, could reduce the hydrogen content. Moshtaghi et al. [17] designed a high-strength martensitic steel by introducing novel metal nanoprecipitates (Nb,V)C as hydrogen traps to suppress HE. The methods above focus on tailoring alloy composition or bulk microstructure. Note that a change in microstructure may compromise the material's strength. For example, the HE resistance of solution-annealed 304 ASS is better than that of the cold-deformed one, but the strength is significantly reduced [18]. To improve HE resistance, surface engineering is another efficient way and is of great interest.

In recent years, the technology of low-temperature carburizing (LTC) has attracted widespread attention. This is a surface thermochemical treatment that can avoid significant modification of the bulk microstructure. It introduces a carbon supersaturated solid solution called "expanded austenite" [19] on the surface without forming carbides.

---

* Corresponding author.
E-mail addresses: yu.cao@chalmers.se, emmy.cao@hotmail.se (Y. Cao).

https://doi.org/10.1016/j.jmrt.2025.05.125
Received 10 January 2025; Received in revised form 28 April 2025; Accepted 16 May 2025

Typically, the content of the interstitial carbon (C) in expanded austenite can reach up to 12 at% [20], which is several orders of magnitude larger than the equilibrium solubility at these temperatures. Michal et al. attributed this colossal supersaturation to para-equilibrium [21]. While substitutionally dissolved atoms are essentially immobile at low treatment temperatures. Within the typical processing time, a high interstitial content of C is obtained. Meanwhile, precipitation is avoided. It is generally accepted that the carburizing temperatures for expanded austenite are lower than 500 °C [20].

Expanded austenite can be formed by both interstitially dissolved carbon and nitrogen. Usually, it exists on the surface with high compressive residual stress due to lattice expansion caused by interstitials [20]. It is ideal for components that require high surface hardness and good resistance to wear, fatigue and corrosion [21–23]. Compared to N stabilized expanded austenite, C stabilized expanded austenite has higher load bearing capacity and toughness, further improved fatigue properties, as well as better thermal stability [24]. It has been found that for ASTM 316Ti steel, the supersaturated austenite layer stabilized by nitrogen decreased hydrogen uptake in the underlying steel substrate due to lowered concentration of diffusible hydrogen in the expanded austenite layer [25]. Hydrogen absorption in 304L austenitic stainless steel has also been reported to be suppressed by low temperature gas carburizing treatment [26]. O. Takakuwa et al. pointed out [27,28] that cavitation peening introduced compressive stress and reduced the hydrogen-assisted fatigue crack growth, attributed to the lowered local hydrogen concentration level ahead of the crack tip. The high compressive residual stress in the expanded austenite has a similar effect, which inhibits hydrogen penetration and initiation and propagation of cracks [26].

So far, only a few studies focused on the effect of LTC on the HE of metastable ASS in recrystallized conditions prior to LTC treatment [26, 29]. Industrially manufactured ASS components are often in cold-worked states. It is well known that cold working introduces a high density of dislocations and martensitic phase transformation in metastable ASS, affecting HE resistance [9–11]. In this study, commercial 304 ASS in a cold-worked condition was subjected to LTC treatment to obtain expanded austenite at the surface. Hydrogen was introduced into the steel using the electrochemical cathodic charging method. Slow strain rate tensile tests were used to examine the effect of LTC treatment on the mechanical behavior and HE of cold worked 304. This work evaluates the potential of alleviating cold-worked 304 austenitic stainless steels from hydrogen embrittlement by LTC treatment. The correlation between HE resistance, microstructure, and hydrogen uptake will be created and discussed.

2. Experimental procedure

2.1. Material and conditions

The material used in the present work was a commercial AISI 304 austenitic stainless steel with a chemical composition of Fe-0.06C-0.39Si-1.58Mn-18.22Cr-8.02Ni-0.33Cu (wt.%). The as-received samples were cold-drawn bars with an area reduction of 20 %, and their mechanical properties are listed in Table 1. Here $Rp_{0.2}$ denotes yield stress at 0.2 % offset and R_m is tensile strength. Low-temperature carburizing was performed by Bodycote using the commercial Kolsterising® K22 process [30]. All the tested materials were treated in a carburizing atmosphere at a low temperature (<500 °C) for several days.

Table 1
Mechanical properties at room temperature of AISI 304 used in this study.

$R_{p0.2}$ (MPa)	R_m (MPa)	Hardness (BHN)	Elongation (%)	Reduction Area (%)
710	820	231	34	75

2.2. Hydrogen charging and slow strain rate tensile (SSRT) tests

The cylindrical tensile specimens were prepared according to ASTM standard (E8M − 04) with the longitudinal axis parallel to the cold-drawing direction. The gauge length and diameter were 25 mm and 5 mm, respectively. Hydrogen charging was performed by electrochemical cathodic method in an aqueous solution of 0.2 mol/L H_2SO_4+ 1 g/L Na_2HAsO_4. Hydrogen was introduced into the tensile bar at a current density of 30 mA/cm^2 for 72 h at 80 ± 5 °C. After hydrogen charging was completed, surface morphologies of the tensile bar were examined and no obvious cracks were found, as shown in Supplementary Fig. S1. The material conditions in this investigation are summarized in Table 2.

The tensile samples were tested immediately after hydrogen charging at a constant slow strain rate of $1 \times 10^{-3}\ s^{-1}$ and $5 \times 10^{-5}\ s^{-1}$ at room temperature using a universal testing machine (Instron 5500R, USA). The strain data in the stress-strain curve was recorded by an extensometer (with a gauge length of 10 mm). All the tests were performed three times to ensure data reliability. In order to evaluate the susceptibility to hydrogen embrittlement, indices δ_L and φ_L, namely relative plasticity loss, as defined in Eqs. (1) and (2), were determined.

$$\delta_L = \frac{\delta_0 - \delta_H}{\delta_0} \times 100\% \tag{1}$$

$$\varphi_L = \frac{\varphi_0 - \varphi_H}{\varphi_0} \times 100\% \tag{2}$$

where δ_0 and δ_H are the total elongation of uncharged and H-charged specimens, respectively. φ_0 and φ_H are area reductions in the percentage of uncharged and H-charged specimens, respectively. In general, higher δ_L or φ_L indicates higher ductility loss, i.e., more susceptible to hydrogen embrittlement.

2.3. Microstructural characterization

Metallographic samples were prepared by mechanical grinding and polishing using OPS (Struers) silica suspension as the final step, and examined by scanning electron microscope (SEM) using a LEO Gemini 1550 FE-SEM. The hardness profiles were obtained on cross-section as a function of depth using a DuraScan 70 G5 micro-Vickers hardness tester with a load of 10 gf. The indentation size was measured by SEM. The hardness was an averaged value from five points. The carbon content in the depth of the carburized layer was measured using JEOL Electron probe microanalyzer (EPMA, JXA-8230). The phase identification was performed on a Bruker D8 Discover X-ray diffractometer equipped with Cu Kα radiation and operated at a voltage of 40 kV and a current of 40 mA. Electron backscatter diffraction (EBSD) was also used to examine the microstructure of the samples before and after tensile tests. It was performed using a LEO Gemini 1550 FE-SEM coupled with an Oxford Nordlys collection system. The step size of EBSD map acquisition was 0.1–1 μm. The accelerating voltage was set at 20 kV, and the working distance was about 14 mm. HKL* Channel 5 data analysis software was used for inverse pole figure (IPF), grain boundary (GB), and phase analysis. The fracture surfaces of tensile specimens were examined by TESCAN MIRA4 FE-SEM. The hydrogen content of the samples was measured by means of thermal desorption spectroscopy (TDS) using Galileo G8 from Bruker. The samples were heated from room

Table 2
Samples used in this study.

Name of samples	Conditions
304	As received cold worked 304
304-H	Cold worked 304 charged with hydrogen
304 LTC	Carburized cold worked 304
304 LTC-H	Carburized cold worked 304 followed by hydrogen charging

temperature (RT) to 800 °C in an infrared quartz tube furnace at a heating rate of 0.5 °C/s.

3. Results

3.1. Initial microstructure

The microstructure of the initial cold-worked 304 is shown in Fig. 1. Austenite grains with typical twin structures had a color gradient in the inverse pole figure (IPF) map, as shown in Fig. 1a, indicating gradient orientations within the grains, characteristic of a deformed structure. The measured austenite grain size (D_γ) was 16.3 ± 8.7 μm. In grain boundary (GB) map (Fig. 1b), the red solid line indicates the low-angle boundary (2–15°), and the black solid line indicates the high-angle boundary (>15°). The high density of small-angle boundaries also revealed deformation within the grains.

Secondary electron micrographs from the cross-section of carburized AISI 304 coupons are shown in Fig. 2a. A continuous distinguishable expanded austenite (γ_c) layer with a thickness of ~22 μm was observed on the steel surface. This carburized layer was featureless compared to the substrate. Slip bands extended into the expanded austenite were observed. Vickers microhardness as a function of depth is shown in Fig. 2b. The surface hardness of the S-phase reaches 1000 HV due to the introduction of supersaturated interstitial carbon. The S-phase was observed to show a high carbon concentration of 1.25 wt% at the top surface in Fig. 2c. The hardness profile followed carbon concentration and gradually decreased with depth. The slow variation of C concentration below the observed expanded layer in the SEM image indicated that the carburization process was controlled by diffusion. The XRD pattern in Fig. 2d reveals the formation of martensite (α′) in the cold-worked 304, the content of which was estimated to be ~25 % by Rietveld Refinement method using Profex software [31]. Interestingly, 304 LTC mainly shows stable austenite (γ_c) peaks. The absence of martensite was supposed to be related to the reversal of martensite to austenite [32,33] transformation due to the thermal energy provided during LTC treatment. Carbon is a strong austenite stabilizer. Supersaturated C induced by LTC is expected to dramatically decrease the martensitic transformation temperature M_s, therefore, austenite is stabilized significantly by this treatment. As a result, deformation-induced martensite transformation is supposed to be inhibited during plastic deformation. This will be confirmed later. For 304 LTC, note the austenite diffraction peaks shift to lower angles due to lattice expansion.

3.2. Effects of low-temperature carburizing and hydrogen uptake on tensile stress-strain response

In order to study the effect of LTC on mechanical properties and HE, two common strain rates (1×10^{-3} s^{-1} and 5×10^{-5} s^{-1}) were used in the tensile test. The detailed mechanical properties including yield strength ($R_{p0.2}$), tensile strength (R_m), uniform elongation (δ_u), total elongation (δ), area reduction (φ) and hydrogen embrittlement index δ_L, φ_L are listed in Table 3.

For hydrogen-free 304, the LTC treatment increased the yield strength and tensile strength of 304 but caused a decrease in uniform and total elongation. The change appeared more obvious at 1×10^{-3} s^{-1}, indicating that 304 LTC has a higher strain-rate sensitivity than as-received 304. Fig. 4 gives the strain hardening rate as a function of strain, derived from true stress-true strain curves, at two strain rates. Notice the true strain corresponding to the onset of necking (maximum uniform deformation) is marked by the symbol " × ". There were two interesting observations. First, LTC treatment gave rise to a significantly higher work hardening rate in the initial stage of plastic deformation, compared to the samples without this treatment. This is related to the factors such as solid solution strengthening due to interstitially dissolved C, and potentially increased density and altered distribution of dislocations. However, the work hardening rate of LTC samples dropped more sharply with strain. It was equivalent to that of the as-received 304 at a true strain of ~13 %. Second, the work hardening rate gradually increased beyond a certain true strain level at the slow strain rate of 5×10^{-5} s^{-1}, which was ~14 % and ~8 % for the samples with and without LTC treatment, respectively. This phenomenon might be associated with strain-induced martensite (SIM) [34,35]. Beyond this strain level, 304 LTC had a lower strain hardening rate, meaning LTC treatment inhibited the martensitic transformation. At a higher strain rate of 1×10^{-3} s^{-1}, no increase in the work hardening rate was observed for 304 LTC. It seemed that the martensitic transformation was inhibited more by LTC treatment at this strain rate.

For hydrogen-charged samples, hydrogen uptake in as-received 304 resulted in a significant increase in yield strength but a decrease in elongation and area reduction. The higher yield strength is due to the increase in dislocation density and martensitic transformation induced by hydrogen charging [36]. This also explained the high hydrogen embrittlement susceptibility index (δ_L>45 % and φ_L>25 %) at both strain rates for cold worked 304. Note that the slow strain rate caused a significant decrease in the uniform elongation of 304-H, indicating an earlier start of the localized deformation (necking). Hydrogen may accelerate the strain localization at a slow strain rate. Interestingly, LTC treatment reduced susceptibility to HE ($\delta_L = 10.4$ % and $\varphi_L = 19.6$ % at 5×10^{-5} s^{-1}) and improved HE resistance significantly at both strain rates, attributed to the inhibited martensite transformation, as stated previously. It is well known that a triaxial stress state is induced after necking, and stress correction is needed to obtain uniaxial stress. However, the stress correction factor is close to 1 when nonuniform deformation is small. A comparison of the work hardening rate of 304 LTC-H and 304 LTC, derived from true stress-true strain curves without correction, can still provide indicative information, at least for the beginning of necking. At the slower strain rate of 5×10^{-5} s^{-1}, the work hardening rate of 304 LTC-H is higher than that of 304 LTC beyond the true strain level ~12 % associated with strain-induced martensite transformation. This confirmed that hydrogen uptake facilitated martensitic transformation. At a higher strain rate of 1×10^{-3} s^{-1}, the quick deformation makes the redistribution of H more difficult. 304

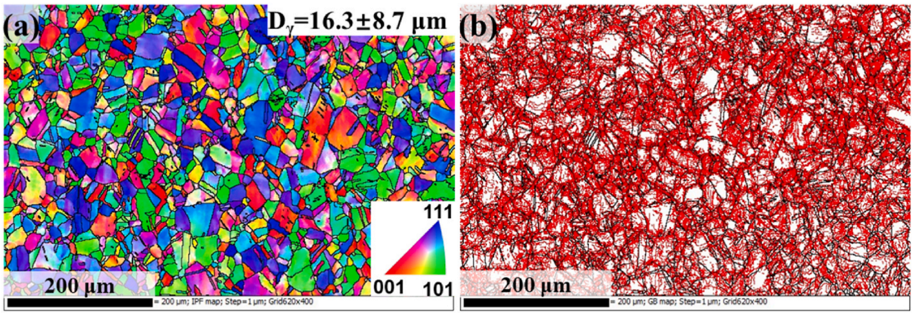

Fig. 1. IPF (a) and GB maps (b) of the cold worked 304.

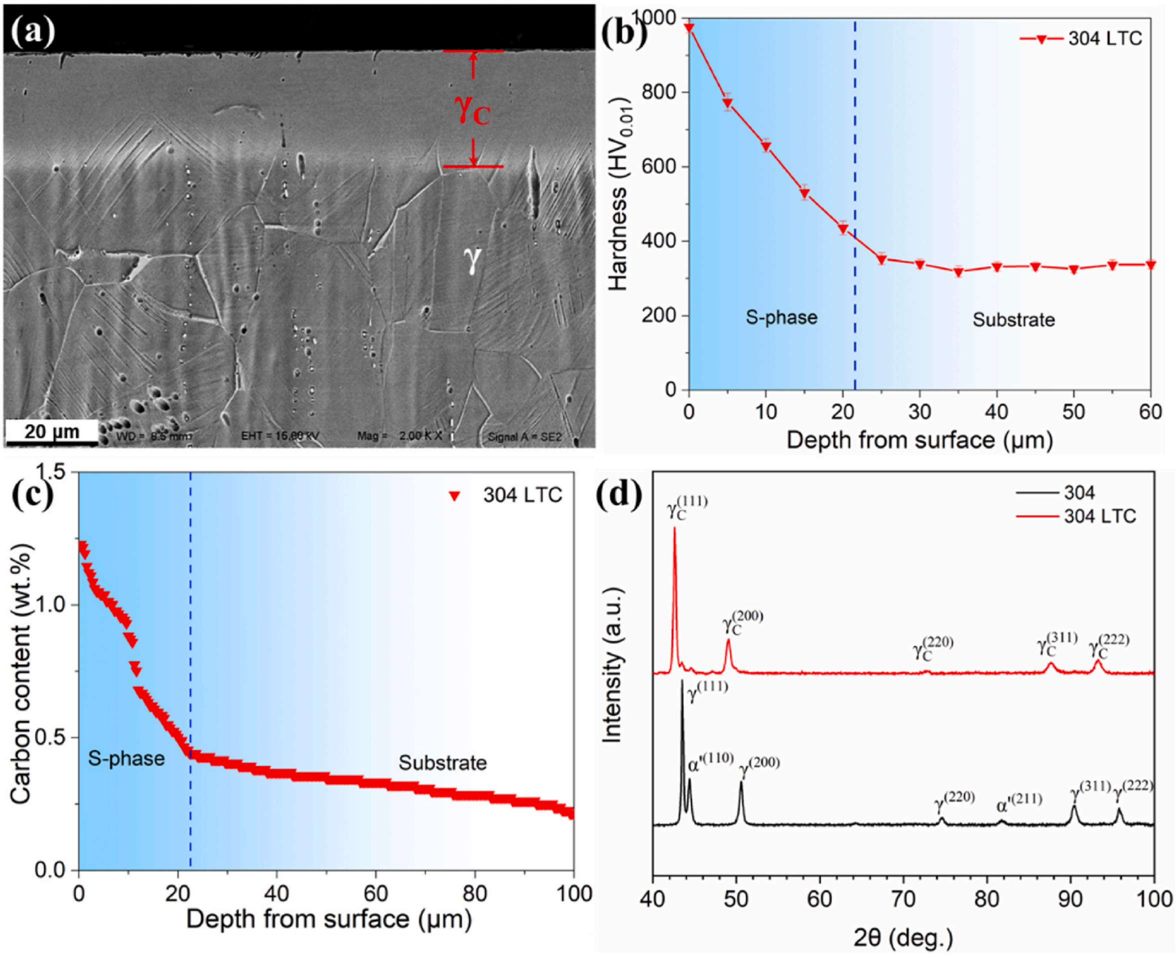

Fig. 2. (a) Secondary electron image, (b) microhardness profiles, (c) carbon profiles, and (d) XRD pattern of the 304 LTC.

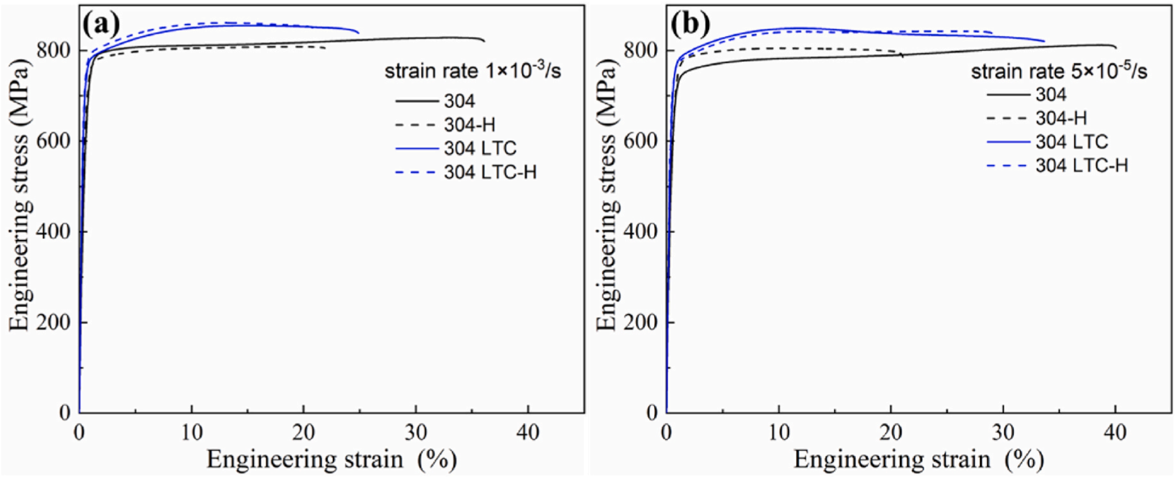

Fig. 3. Tensile stress-strain curves of specimens at different strain rates. (a) 1×10^{-3}/s and (b) 5×10^{-5}/s.

LTC-H showed a continuous decrease in work hardening rate.

Low temperature carburizing on cold worked 304 provided excellent mechanical properties including improved tensile strength and significantly reduced hydrogen-induced ductility loss. Considering that cold-worked 304 is often used in industrial applications, the results of this study are of significant technical importance.

3.3. Fracture morphology

Fig. 5 shows the fracture surface of the 304 and 304 LTC in both H-free and H-charged conditions. The as-received 304 had a completely ductile fracture characteristic, as demonstrated by the well-defined central dimples and surrounding shear regions throughout the whole fracture surface with prominent necking (Fig. 5a). The surface of 304 LTC shows pineapple-peel-like structures as shown in Fig. 5b, as a

Table 3
Mechanical properties of the specimens with and without hydrogen uptake.

Sample	Strain rate s^{-1}	$R_{p0.2}$ (MPa)	R_m (MPa)	δ_u(%)	δ (%)	φ (%)	δ_L (%)	φ_L (%)
304	1×10^{-3}	589 ± 11	809 ± 6	32.0 ± 0.3	53.2 ± 0.6	78.5 ± 0.5	46.7	27.0
304-H		681 ± 13	808 ± 7	20.1 ± 0.5	28.4 ± 0.1	57.3 ± 0.4		
304 LTC		733 ± 12	861 ± 5	14.0 ± 0.4	38.8 ± 0.2	76.5 ± 0.5	11.9	22.0
304 LTC-H		729 ± 11	855 ± 3	12.3 ± 0.3	34.2 ± 0.7	59.7 ± 0.8		
304	5×10^{-5}	609 ± 10	812 ± 3	38.6 ± 0.7	53.8 ± 0.3	77.5 ± 0.5	45.7	33.9
304-H		692 ± 13	804 ± 2	10.5 ± 0.6	29.2 ± 0.6	51.2 ± 0.4		
304 LTC		711 ± 11	842 ± 5	14.2 ± 0.5	42.4 ± 0.5	77.0 ± 0.3	10.4	19.6
304 LTC-H		703 ± 12	848 ± 3	12.5 ± 0.6	38.0 ± 0.2	61.9 ± 0.4		

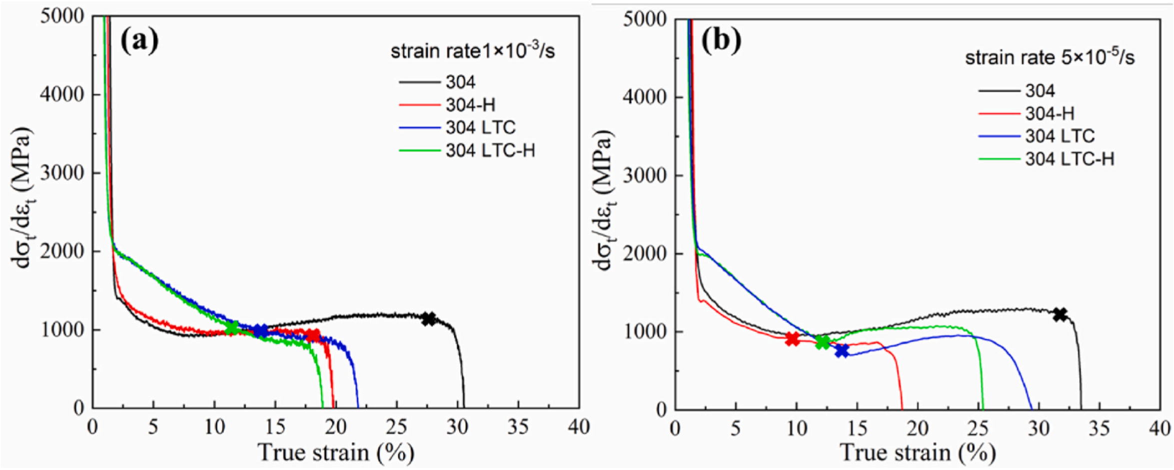

Fig. 4. Strain-hardening rate as a function of strain at different strain rates. (a) 1×10^{-3}/s and (b) 5×10^{-5}/s. True strains corresponding to necking (maximum uniform deformation) under each condition are marked by the symbol " × ".

consequence of reduced ductility. The shear region showed rough tears. In the local high-magnification images, the center region of 304 LTC shows fine dimples (Fig. 5b_1). Elongated dimples were observed on the shear lips of both 304 and 304 LTC samples (Fig. 5a_2 & b_2). Overall, the fracture surfaces of H-charged samples were flatter from macroscopic observation. Two different regions with varied features (Fig. 5c and d) were displayed, i.e., a brittle layer at the edge (Fig. 5c_2 & d_2) and a ductile region with dimples in the sample interior (Fig. 5c_1 & d_1). In addition, the final fracture area was larger than that of the H-free samples, i.e., smaller area reduction. Apparently, hydrogen uptake resulted in the premature fracture of the sample. The high-magnification images of Fig. 5a_1 and b_1 exhibited fine and deep dimples in the H-free samples, while the H-charged samples possessed shallower dimples, as shown in Fig. 5c_1 and d_1. In hydrogen-enhanced localized plasticity mechanism [37], hydrogen accelerates dislocation mobility, promotes the initiation and agglomeration of micropores, and thus forms shallower dimples. Interestingly, in the brittle layer at the edge of the H-charged sample, quasi-cleavage morphology was observed (Fig. 5c_2 & d_2), which was completely different from the H-free samples. Notice that electrochemical hydrogen charging led to extremely high hydrogen concentration in the surface region, forming a hydrogen supersaturated solid solution. The interaction of hydrogen and stress gave rise to quasi-cleavage characteristics. The brittle layer thickness of 304-H (~175 μm) was larger than that of 304 LTC-H (~137 μm). This was attributed to the suppression of deformation induced martensitic transformation by LTC treatment. Generally, martensite has a higher hydrogen diffusivity and consequently larger susceptibility to HE.

3.4. *Initiation and propagation of cracks*

To examine hydrogen-induced cracking, samples were cut along the longitudinal direction after the tensile tests. Fig. 6 shows the morphology of the cross-section. As-received 304 showed necking without obvious crack at the edge (Fig. 6a). For 304 LTC, besides necking, micro cracks were observed at the edge, as shown in the inset of Fig. 6b. This was consistent with the pineapple peel appearance in Fig. 5b. The extremely high hardness of expanded austenite made cracking easier during plastic deformation [38]. However, the crack length remained small in the order of micrometers. In the H-charged samples, as shown in Fig. 6c and d, larger cracks were observed at the edge. Hydrogen uptake promoted crack initiation and propagation under tensile load, leading to cracking of the brittle layer. Note that the open cracks of the 304 LTC-H were shallower and smaller than those of the 304-H, indicating that LTC treatment inhibited the initiation and propagation of hydrogen-assisted cracks. Interestingly, the final fracture was at an angle of ~45° with respect to the tensile direction. The primary cracks tended to propagate along the plane of maximum shear stress, resulting in the characteristic 45° fracture surface.

The microstructure near the fracture surface on the longitudinal section of the H-charged samples was further examined, as shown in Fig. 7. For 304-H, the crack started from the edge and propagated nearly perpendicular to the tensile direction towards the internal zone (Fig. 7a_1). It is well known that high hydrogen concentration on the surface can induce cracks under load. Small cracks could also be formed by aggregation and growth of microvoids beneath the surface. These cracks could be connected afterwards. Fine fragmented grains due to heavy deformation were observed from the IPF map (Fig. 7a_2). The phase map showed dominant martensite α' in 304-H. For 304-H, cracking occurred preferentially within the α'grains or its grain boundaries, as marked with white dashed lines (Fig. 7a_3). There was an interesting observation on orientation-related phase transformation. The <001> orientation was found to have stable γ austenite after undergoing deformation, while the <110> orientation showed α' martensite. Generally, the slip system in fcc austenite is {111}/<110>.

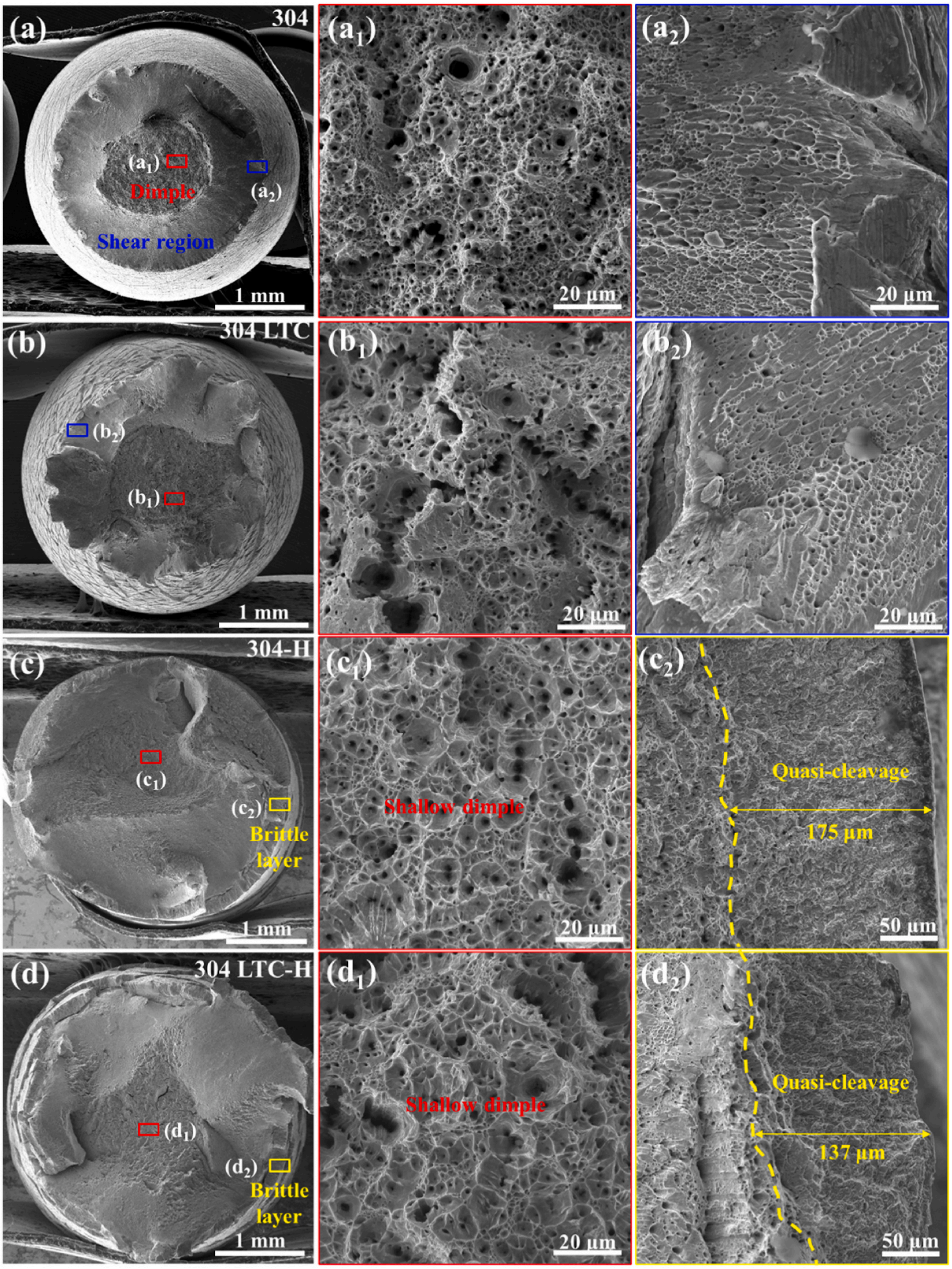

Fig. 5. SEM fracture morphologies of samples in different conditions (a) 304, (b) 304 LTC, (c) 304-H and (d) 304 LTC-H. The middle column (a_1-d_1) is from the middle of the sample, while the right column (a_2-d_2) is from the edge of the sample.

The <110> orientation is prone to slip-induced martensite while <001> is the most difficult. Compared to 304-H, 304 LTC-H exhibits fewer cracks, as shown in Fig. 7b_1. The grains are dominated by < 111> and <001> along the tensile direction (Fig. 7b_2). Since austenite is stabilized by supersaturated carbon, only a small amount of α' was observed in the substrate after tensile deformation (Fig. 7c_3). It is worth noting that the α' content of 304 LTC-H is significantly lower than that of 304-H, confirming that LTC treatment inhibits martensitic transformation. This was consistent with the results in section 3.2 and can explain the improved hydrogen embrittlement resistance after LTC treatment.

4. Discussion

In this study, expanded austenite was introduced into cold-worked 304 ASS to improve HE resistance through LTC treatment. The improved mechanical properties and HE resistance are closely related to the microstructure and hydrogen uptake, as discussed below.

4.1. Effect of LTC treatment on tensile properties

Low temperature carburizing is performed below ~500 °C for dozens of hours [20,21]. During LTC treatment, two fundamental

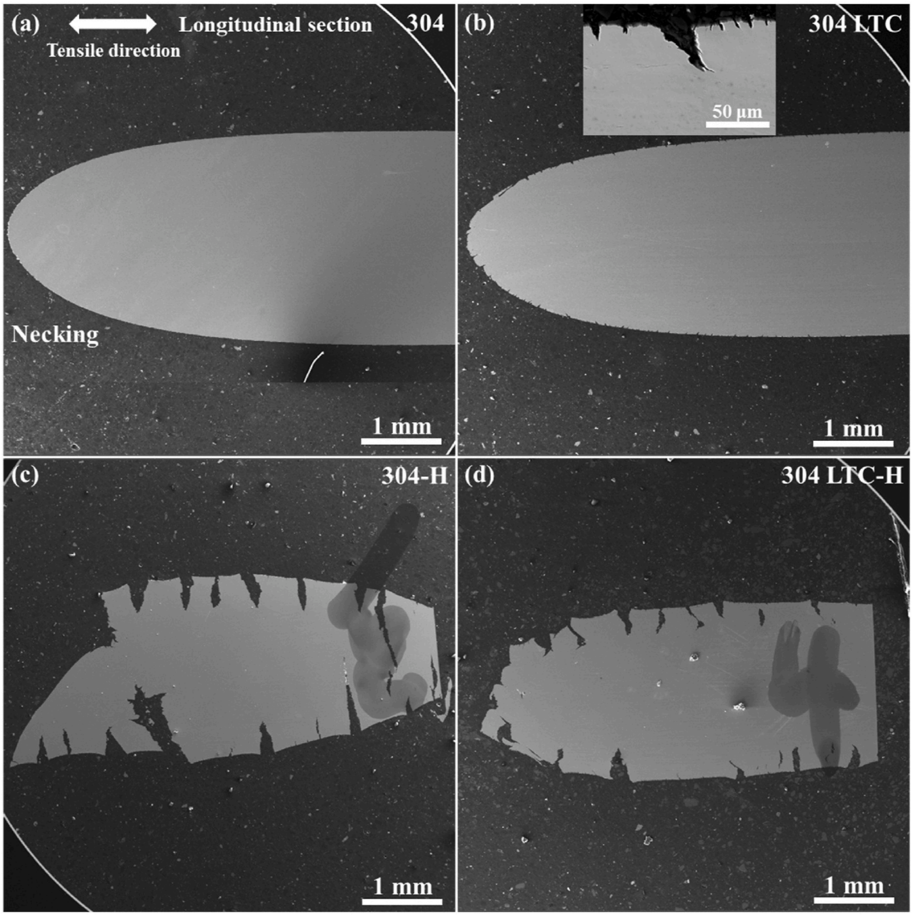

Fig. 6. Morphology of the cross-section along the longitudinal direction after tensile testing of samples in different conditions (a) 304, (b) 304 LTC, (c) 304-H and (d) 304 LTC-H.

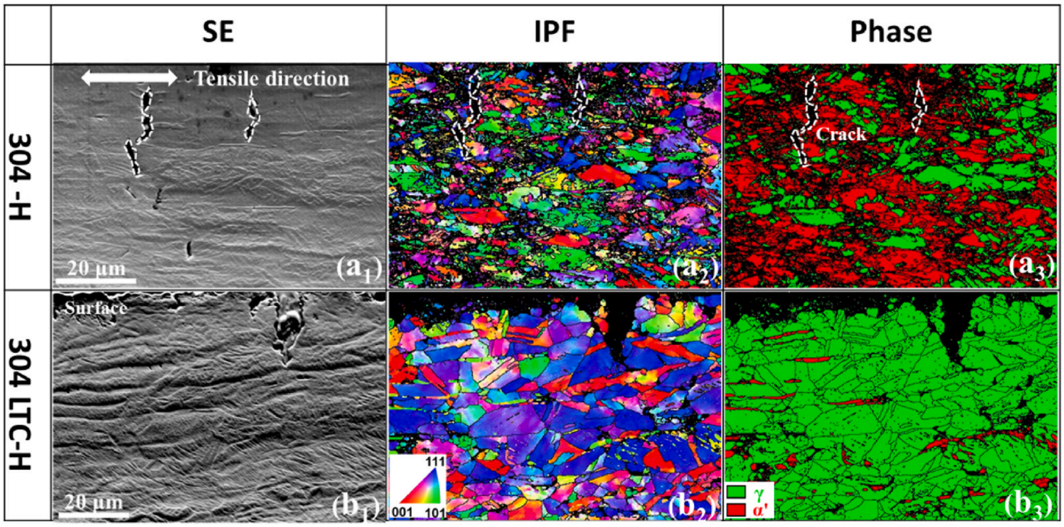

Fig. 7. Microstructures of the H-charged samples on the longitudinal section close to the fracture surface.

microstructural changes occurred: i) formation of a carbon supersaturated solid solution with extremely high hardness in the surface region, and ii) recovery caused by the thermal energy provided. Some literature reported [32,33] that recovery in this temperature range may cause martensite to revert to austenite. Interstitial carbon reduces the transformation temperature M_s and thermodynamic stability of martensite. However, recrystallization will not occur at such a low temperature. Consequently, the change in mechanical properties due to recovery is limited. Microstructural examinations by optical microscope and SEM showed no changes in the center of the sample with and without LTC. No softening was revealed there by the hardness measurement. Increased yield and tensile strength but decreased elongation at both strain rates, as shown in Fig. 3 and Table 3 are attributed to the formation of expanded austenite in the surface region.

Carbon as an interstitial atom provides a solution-strengthening effect. The supersaturated interstitial carbon introduced by LTC treatment causes severe lattice distortion [39,40], as indicated by the broadened and shifted diffraction peaks from austenite in Fig. 2d. The induced stress field around the solute atoms hinders the movement of dislocations, improving strength. LTC treatment may also introduce a high density of dislocations, and thus increasing the strengths. Although the expanded austenite layer shown in the SEM image in Fig. 2 a) is only ~22 μm, the influence on the mechanical properties is large. Expanded austenite is a supersaturated solid solution with a carbon gradient. Carbon diffusion during LTC treatment makes the carbon concentration below this layer higher than that of the uncarburized sample. Extrapolating the carbon profile in Fig. 2c suggests that the carbon diffusion zone is thicker than 200 μm. The hardness of the surface region is much higher than that of the substrate. During tensile deformation, the hard surface layer restricts the plastic deformation of the softer austenite in the substrate. This constraint effect leads to an increase in the strength. Second, the mismatch in hardness between the expanded austenite and the substrate causes stress redistribution, thereby delaying the onset of yielding. Moreover, the expanded austenite causes compressive residual stresses due to lattice expansion, which offsets the applied tensile load and thus delays plastic deformation. In addition, carburization at low temperatures introduces a strain gradient. Dislocations are accumulated not only in the expanded austenite but also in the underlying austenite substrate, contributing to the overall improved strength.

As a natural consequence of increased strength, ductility is decreased for 304 LTC. For as-received 304, the strain-induced martensitic transformation occurs during tensile deformation, leading to transformation-induced plasticity (TRIP). Ryoo et al. [41] reported that the martensite content in 304 ASS increased significantly from 2.5 % to 21 % when the tensile strain increased from 20 % to 50 %. For 304 LTC, low temperature carburizing stabilizes austenite and inhibits martensite formation, suppressing the TRIP effect with consequently reduced ductility, at least in the surface region. Notice that the carbon concentration gradient arising from the diffusional LTC process causes a compressive stress gradient. The largest stress is on the surface. For a ~30 μm thick carburized layer, the surface compressive residual stress can be as high as ~ -2.2 GPa [42]. This leads to early crack initiation and propagation in the surface region during the uniaxial tension test. The stress-induced cracking in 304 LTC is confirmed in Fig. 6b. Early cracking of the outermost layer greatly reduces the ductility. This is consistent with the findings reported by Jiang et al. [42].

4.2. Effect of LTC treatment on HE

As revealed in Fig. 3 and Table 3, hydrogen uptake in as-received 304 results in a significant decrease in elongation and area reduction. This is related to hydrogen-facilitated martensitic transformation in the steel, which affects HE resistance negatively. Hydrogen uptake promotes deformation-induced martensitic transformation primarily by affecting the thermodynamics and kinetics of the transformation. Hydrogen increases the mobility of dislocations, leading to higher strain localization [37]. This promotes stress-assisted martensitic nucleation at dislocation pile-ups and grain boundaries. Hydrogen also reduces the stacking fault energy of austenitic steels [43], making it easier for partial dislocations to move and create stacking faults, which serve as nucleation sites for martensite.

It is shown from SSRT results that LTC treatment significantly improves the HE resistance of cold worked 304. The LTC treatment introduces stable expanded austenite, surface residual compressive stress and a recovered microstructure in the core. These factors have positive effects on suppressing HE. Supersaturated carbon in expanded austenite increases the stacking fault energy (SFE) by changing atomic interactions [20]. Higher SFE promotes planar dislocation slip rather than deformation-induced phase transformation. This prevents deformation twinning and strain-induced martensite formation [9–11]. Austenite is therefore stabilized in the surface region, which is the first place for hydrogen uptake. Austenite has been widely reported to have excellent resistance to HE due to its extremely low hydrogen diffusivity [1,5]. The dominant austenite in 304 LTC-H inhibits crack propagation (Fig. 6d) and reduces the thickness of the quasi-cleavage layer (Fig. 5d$_2$). Surface residual stress is another important factor affecting HE. Hydrostatic stress can lead to hydrogen enrichment at the crack tip or elastic-plastic boundary [44,45]. Tensile residual stress can accelerate hydrogen uptake, while compressive residual stress can reduce hydrostatic stress and lower the distance between atoms, thereby inhibiting hydrogen diffusion [46]. Takakuma et al. introduced compressive stress in 316L ASS by cavitation peening to reduce hydrogen-assisted fatigue crack growth [27,28]. Numerical simulations demonstrated that compressive stress reduced the local hydrogen concentration level in front of the crack tip and that the higher the compressive stress generated, the lower the hydrogen concentration [28]. Brass et al. [47] believed shot peening of low-carbon steel made the distribution of hydrogen more uniform in the cold-worked layer produced at the surface, and the compressive stress inhibited the initiation of cracks. In this study, LTC introduced compressive stress in the expanded austenite on the surface, which can act as a barrier inhibiting hydrogen diffusion. In addition, the accompanied recovery during carburizing reduces internal tensile stress caused by previous cold working and overall dislocation density in the underlying substrate, which reduces hydrogen-induced cracking.

4.3. Effect of phases on hydrogen diffusivity and uptake

As shown in Fig. 5, a brittle layer with quasi-cleavage morphology was observed on the surface after the tensile test for samples with hydrogen uptake (304-H and 304 LTC-H), the thickness of which depends on hydrogen diffusivity. 304 LTC-H has a thinner brittle layer compared to 304-H, indicating that LTC treatment reduces hydrogen penetration depth. The general low hydrogen diffusivity in austenite makes it reasonable to assume a hydrogen concentration gradient from the surface to the inner region during hydrogen charging, with the highest concentration on the surface (constant). The diffusion flux and the concentration of H at some particular location of the steel vary with time. Fick's second law can be used to describe the diffusion behavior. Assuming a semi-infinite solid, the hydrogen concentration at depth Z during hydrogen charging can be expressed by Eq. (3).

$$C(z,t) = C_i + (C_s - C_i)\left\{1 - \mathrm{erf}\left(\frac{z}{2\sqrt{D_{app}t}}\right)\right\} \tag{3}$$

Where z: depth from the surface.

t: charging time.

C(z,t): hydrogen concentration at depth z after time t.

C_i: initial hydrogen concentration in the steel.

C_s: saturated hydrogen concentration at the surface during hydrogen charging.

Xu et al. [48] reported that when $C_z = 0.12C_s$, the hydrogen penetration depth (z) is approximately equal to the brittle layer thickness. In this study, 304-H and 304 LTC-H have the same charging time of 72 h. The brittle layers are 175 and 137 μm for 304-H and 304 LTC-H, respectively. Assuming the initial hydrogen concentration C_i in the steel is 0, hydrogen diffusivity could be estimated roughly by using Eq. (3). The calculated D_{app} for 304-H and 304 LTC-H are 2.44×10^{-14} m^2/s and 1.49×10^{-14} m^2/s, respectively. Obviously, LTC treatment reduces the hydrogen diffusivity of 304. Li et al. [29] also reported that at 300 °C, the hydrogen diffusivity of 304 LTC is lower than that of 304.

One factor that affects hydrogen diffusivity is the crystal structure of the phases. Hydrogen diffusivity differs significantly in martensite and austenite phases. Martensite has a higher hydrogen diffusivity than austenite, making it more susceptible to HE. Sezgin et al. [49] reported that the hydrogen diffusivity in α′ is 5 orders of magnitude higher than that of γ at 143 °C. For the metastable 304 ASS, deformation induces martensite transformation. In this work, as received 304 has a small amount of α’ due to cold-drawing process. After hydrogen uptake and tensile deformation, Fig. 7a$_3$ verifies that α’ is dominant close to the fracture surface for 304-H. The high hydrogen diffusivity and low solubility of martensite cause hydrogen to accumulate within martensite and at martensite/austenite boundaries. Localized stress concentrations at high hydrogen pressure facilitate the initiation and propagation of cracks, leading to premature fracture of the steel [50]. On the other hand, 304 LTC has stable austenite, as shown in Fig. 2d. The difference in phase constituents explains the varied hydrogen diffusivity and HE resistance. After the tensile test, the microstructure of 304 LTC-H is mainly γ austenite (Fig. 7b$_3$) with fewer cracks, because the deformation-induced martensite transformation is inhibited by C stabilized austenite.

Hydrogen content also affects HE. Hydrogen exists in the microstructure as diffusible hydrogen and trapped hydrogen. Thermal desorption analysis as a function of temperature is useful for detecting diffusible hydrogen. Fig. 8 shows the hydrogen desorption spectra obtained at a constant heating rate of 0.5 °C/s for 304-H and 304 LTC-H. Both samples showed two distinct peaks, which appeared in the temperature range of 150–180 °C (Peak 1) and 350–380 °C (Peak 2), respectively. Table 4 summarizes the obtained hydrogen content and peak temperature for 304-H and 304 LTC-H. Both peak 1 and peak 2 of 304 LTC-H were lower than those of 304-H. The total hydrogen content of the 304-H is 3.2 ppm, approximately twice that of 304 LTC-H (1.7 ppm). This means that LTC treatment inhibits hydrogen uptake and thus reduces hydrogen content. It is known that peak 1 is due to the capture of diffusible hydrogen by the lattice, dislocations, grain boundaries, etc. [51], while peak 2 at a higher temperature is for non-diffusible hydrogen captured by locations such as twin boundaries and incoherent precipitates [17].

For as received 304, martensite transformation occurs during cold working and hydron charging. The change in crystal structure from FCC (austenite) to BCC (martensite) is achieved by a deformation of the parent phase. As a result, martensite undergoes transformation twinning and/or slipping. The typical substructure of martensite is transformation twins and densified dislocations. Compared to 304 LTC with expanded austenite, 304 has a considerably higher martensite content, as revealed in Fig. 2d. Peak 2 for 304-H is significantly higher than that for 304 LTC-H (Fig. 8). This may correspond to hydrogen in the martensite, associated with its substructure.

5. Conclusions

In this study, the mechanical properties and hydrogen embrittlement of low-temperature carburized cold-worked 304 austenitic stainless steel were investigated and correlated with the microstructure. The conclusions obtained are summarized as follows.

(1) Low-temperature carburizing introduced a 22 μm thick expanded austenite at the surface, which increases the strength and surface hardness of cold-worked 304 but reduces the elongation. Compared to 304, 304 LTC showed a higher strain rate sensitivity and an increased strain hardening rate, but the difference in strain hardening rate became smaller with strain.
(2) Hydrogen uptake caused loss of ductility. The elongation loss of 304-H was ~46 %. After LTC treatment, the ductility loss due to hydrogen uptake was much smaller (the elongation loss was ~11 %), and HE resistance was significantly improved.
(3) A quasi-cleavage layer with some cracks formed on the surface of steel with hydrogen uptake. 304-H showed higher surface crack density and a thicker quasi-cleavage layer compared to 304 LTC-H.

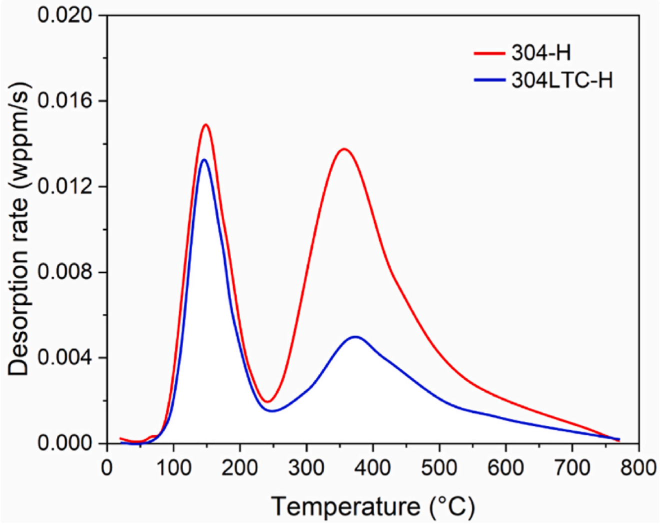

Fig. 8. H desorption rate curves obtained from thermal desorption spectra of 304-H and 304 LTC-H. All samples were hydrogen charged at 80 °C for 5 h with a current density of 30 mA/cm^2 after exposure for 48 h.

Table 4
Peak temperatures and concentrations of desorbed H measured from the thermal desorption spectra.

Sample	Total H (wppm)	Peak 1 H (wppm)	Peak 2 H (wppm)	Peak temperature1 (°C)	Peak temperature 2 (°C)
304-H	3.2	1.2	2.0	168	359
304 LTC-H	1.7	1.0	0.7	165	372

(4) The higher sensitivity to hydrogen embrittlement of 304-H was due to the higher martensite content and more hydrogen uptake. For 304 LTC-H, stable austenite with compressive stress was dominant in the surface region, reducing hydrogen diffusion and uptake, thus showing improved hydrogen embrittlement resistance.
(5) Expanded austenite formed by low temperature carburizing is a stable austenite that can inhibit martensitic phase transformation, improve strength, provide excellent resistance to hydrogen embrittlement, and act as a hydrogen diffusion barrier.

Declaration of competing interest

The authors declare that they have no known competing financial interests or personal relationships that could have appeared to influence the work reported in this paper.

Acknowledgments

This work was financed by Sweden’s innovation agency (2021-01908), competence centre TechForH2 hosted by Chalmers University of Technology and financially supported by the Swedish Energy Agency (P2021-90268) and the member companies Volvo, Scania, Siemens Energy, GKN Aerospace, PowerCell, Oxeon, RISE, Stena Rederier AB, Johnsson Matthey and Insplorion, and China Scholarship Council.

Appendix A. Supplementary data

Supplementary data to this article can be found online at https://doi.org/10.1016/j.jmrt.2025.05.125.

References

[1] Qiu Y, Yang H, Tong L, Wang L. Research progress of cryogenic materials for storage and transportation of liquid hydrogen. Metals 2021;11(7):1101.

[2] Völkl J, Alefeld G. Diffusion of hydrogen in metals, hydrogen in metals I: basic properties. Berlin: Springer Verlag; 1978. p. 197–226.

[3] Louthan JrMR, Derrick RG. Hydrogen transport in austenitic stainless steel. Corros Sci 1975;15(6–12):565–77.

[4] Dwivedi SK, Vishwakarma M. Hydrogen embrittlement in different materials: a review. Int J Hydrogen Energy 2018;43:21603–16.

[5] Perng TP, Altstetter CJ. Comparison of hydrogen gas embrittlement of austenitic and ferritic stainless steels. Metall Trans A 1987;18:123–34.

[6] Nickel C. ASM specialty handbook, vol. 22. International Materials Park, OH: ASM; 2000. 44073–0002.

[7] Plaut RL, Herrera C, Escriba DM, Rios PR, Padilha AF. A short review on wrought austenitic stainless steels at high temperatures: processing, microstructure, properties and performance. Mater Res 2007;10:453–60.

[8] Llewellyn DT. Work hardening effects in austenitic stainless steels. Mater Sci Technol 1997;13(5):389–400.

[9] Rozenak P, Eliezer D. Phase changes related to hydrogen-induced cracking in austenitic stainless steel. Acta Metall 1987;35:2329–40.

[10] Rozenak P. Stress induce martensitic transformations in hydrogen embrittlement of austenitic stainless steels. Metall Mater Trans 2014;45:162–78.

[11] Zhang HY, Zheng LW, Wang T, Lv WJ, Shi QX, Ma JY, Misra RDK. Interrelationship between hydrogen and α′-martensite of SUS 304 austenitic stainless steel revealed by tensile tests. Mater Sci Eng, A 2022;831:142169.

[12] Li X, Ma X, Zhang J, Akiyama E, Wang Y, Song X. Review of hydrogen embrittlement in metals: hydrogen diffusion, hydrogen characterization, hydrogen embrittlement mechanism and prevention. Acta Metall Sin 2020;33:759–73.

[13] Liu MA, Rivera-Díaz-del-Castillo PE, Barraza-Fierro JI, Castaneda H, Srivastava A. Microstructural influence on hydrogen permeation and trapping in steels. Mater Des 2019;167:107605.

[14] Kim KS, Kang JH, Kim SJ. Nitrogen effect on hydrogen diffusivity and hydrogen embrittlement behavior in austenitic stainless steels. Scripta Mater 2020;184:70–3.

[15] Fan YH, Zhang B, Wang JQ, Han EH, Ke W. Effect of grain refinement on the hydrogen embrittlement of 304 austenitic stainless steel. J Mater Sci Technol 2019;35(10):2213–9.

[16] Zhang HY, Hu J, Meng XM, Sun Y, Wang T, Lv WJ, Zheng LW. Effect of deformation microstructures on hydrogen embrittlement sensitivity and failure mechanism of 304 austenitic stainless steel: the significant role of rolling temperature. J Mater Res Technol 2022;17:2831–46.

[17] Moshtaghi M, Maawad E, Bendo A, Krause A, Todt J, Keckes J, Safyari M. Design of high-strength martensitic steels by novel mixed-metal nanoprecipitates for high toughness and suppressed hydrogen embrittlement. Mater Des 2023;234:112323.

[18] Zhang HY, Li YM, Liang W, Zheng LW. Observation of hydrogen diffusion channel and hydrogen trap in 304 austenitic stainless steel. Mater Lett 2021;290:129453.

[19] Sun Y, Li X, Bell T. Structural characteristics of low temperature plasma carburised austenitic stainless steel. Mater Sci Technol 1999;15:1171–8.

[20] Borgioli F. From austenitic stainless steel to expanded austenite-S phase: formation, characteristics and properties of an elusive metastable phase. Metals 2020;10:187.

[21] Michal GM, Ernst F, Kahn H, Cao Y, Oba F, Agarwal N, Heuer AH. Carbon supersaturation due to paraequilibrium carburization: stainless steels with greatly improved mechanical properties. Acta Mater 2006;54:1597–606.

[22] Ceschini L, Minak G. Fatigue behaviour of low temperature carburised AISI 316L austenitic stainless steel. Surf Coating Technol 2008;202:1778–84.

[23] Sun Y, Li X, Bell T. Low temperature plasma carburising of austenitic stainless steels for improved wear and corrosion resistance. Surf Eng 1999;15(1):49–54.

[24] Dong H. S-phase surface engineering of Fe-Cr, Co-Cr and Ni-Cr alloys. Int Mater Rev 2010;55(2):65–98.

[25] Zakroczymski T, Flis J, Lukomski N, Mankowski J. Entry, transport and absorption of hydrogen in low-temperature plasma nitrided austenitic stainless steel. Acta Mater 2001;49:1929–38.

[26] Jiang Y, Wu Q, Wang Y, Zhao J, Gong J. Suppression of hydrogen absorption into 304L austenitic stainless steel by surface low temperature gas carburizing treatment. Int J Hydrogen Energy 2019;44:24054–64.

[27] Takakuwa O, Soyama H. Suppression of hydrogen-assisted fatigue crack growth in austenitic stainless steel by cavitation peening. Int J Hydrogen Energy 2012;37:5268–76.

[28] Takakuwa O, Nishikawa M, Soyama H. Numerical simulation of the effects of residual stress on the concentration of hydrogen around a crack tip. Surf Coat Technol 2012;206:2892–8.

[29] Li Y, Li W, Zhu X, Zhou H, Jin X. Mechanism of improved hydrogen embrittlement resistance of low-temperature plasma carburised stainless steel. Surf Eng 2018;34:189–92.

[30] Rey O, Kolsterising P Jacquot. Hardening of austenitic stainless steel. Surf Eng 2002;18:412–4.

[31] Doebelin N, Kleeberg R. Profex: a graphical user interface for the Rietveld refinement program BGMN. J Appl Crystallogr 2015;48:1573–80.

[32] Panov D, Kudryavtsev E, Chernichenko R, Smirnov A, Stepanov N, Simonov Y, Salishchev G. Mechanisms of the reverse martensite-to-austenite transformation in a metastable austenitic stainless steel. Metals 2021;11(4):599.

[33] Yang DP, Wu D, Yi HL. Reverse transformation from martensite into austenite in a medium-Mn steel. Scripta Mater 2019;161:1–5.

[34] Soares GC, Gonzalez BM, de Arruda Santos L. Strain hardening behavior and microstructural evolution during plastic deformation of dual phase, non-grain oriented electrical and AISI 304 steels. Mater Sci Eng, A 2017;684:577–85.

[35] Moat RJ, Zhang SY, Kelleher J, Mark AF, Mori T, Withers PJ. Work hardening induced by martensite during transformation-induced plasticity in plain carbon steel. Acta Mater 2012;60:6931–9.

[36] Wang D, Lu X, Wan D, Li Z, Barnoush A. In-situ observation of martensitic transformation in an interstitial metastable high-entropy alloy during cathodic hydrogen charging. Scripta Mater 2019;173:56–60.

[37] Birnbaum HK, Sofronis P. Hydrogen-enhanced localized plasticity—a mechanism for hydrogen-related fracture. Mater Sci Eng, A 1994;176:191–202.

[38] Souza RMD, Ignat M, Pinedo CE, Tschiptschin AP. Structure and properties of low temperature plasma carburized austenitic stainless steels. Surf Coating Technol 2009;204:1102–5.

[39] Wang Z, Baker I, Cai Z, Chen S, Poplawsky JD, Guo W. The effect of interstitial carbon on the mechanical properties and dislocation substructure evolution in Fe40.4Ni11.3Mn34.8Al7.5Cr6 high entropy alloys. Acta Mater 2016;120:228–39.

[40] Hummelshøj TS, Christiansen TL, Somers MA. Lattice expansion of carbon-stabilized expanded austenite. Scripta Mater 2010;63(7):761–3.

[41] Ryoo DY, Kang N, Kang CY. Effect of Ni content on the tensile properties and strain-induced martensite transformation for 304 stainless steel. Mater Sci Eng, A 2011;528:2277–81.

[42] Jiang Y, Li Y, Peng Y, Gong J. Mechanical properties and cracking behavior of low-temperature gaseous carburized austenitic stainless steel. Surf Coating Technol 2020;403:126343.

[43] Zhou XW, Nowak C, Skelton RS, Foster ME, Ronevich JA, San Marchi C, Sills RB. An Fe–Ni–Cr–H interatomic potential and predictions of hydrogen-affected stacking fault energies in austenitic stainless steels. Int J Hydrogen Energy 2022;47(1):651–65.

[44] Liang Y, Sofronis P, Dodds Jr RH. Interaction of hydrogen with crack-tip plasticity: effects of constraint on void growth. Mater Sci Eng, A 2004;366(2):397–411.

[45] Krom AH, Koers RW, Bakker A. Hydrogen transport near a blunting crack tip. J Mech Phys Solid 1999;47(4):971–92.

[46] Li XF, Zhang J, Ma MM, Song XL. Effect of shot peening on hydrogen embrittlement of high strength steel. J Miner Metall Mater 2016;23:667–75.

[47] Brass AM, Chene J, Anteri G, Ovejero-Garcia J, Castex L. Role of shot-peening on hydrogen embrittlement of a low-carbon steel and a 304 stainless steel. J Mater Sci 1991;26:4517–26.

[48] Lu X, Wang D, Wan D, Zhang ZB, Kheradmand N, Barnoush A. Effect of electrochemical charging on the hydrogen embrittlement susceptibility of alloy 718. Acta Mater 2019;179:36–48.

[49] Sezgin JG, Takatori D, Yamabe J. Experimental and simulation study on effective hydrogen diffusivity of cold-worked Type-304 austenitic stainless steel. In: Pressure vessels and piping conference. ASME; 2019.

[50] Zhang L, An B, Fukuyama S, Iijima T, Yokogawa K. Characterization of hydrogen-induced crack initiation in metastable austenitic stainless steels during deformation. J Appl Phys 2010;108:063526.

[51] So KH, Kim JS, Chun YS, Park K-T, Lee Y-K, Lee CS. Hydrogen delayed fracture properties and internal hydrogen behavior of a Fe-18Mn-1.5Al-0.6C TWIP steel. ISIJ Int 2009;49:1952–9.